Supplementary Information for: Tunable drag drop via flow-induced snap-through in origami

Rishabh Nain[1*], Tom Marzin[1,2], and Sophie Ramananarivo[1]

[1]Laboratoire d'Hydrodynamique, CNRS, École polytechnique, Institut Polytechnique de Paris, 91120 Palaiseau, France,
[2]Chemical and Biological Engineering, Princeton University, NJ 08544, United States

Contents

1 Experimental methods

1.1 Fold stiffness

To measure fold stiffness, a prototype of a single crease was designed using the manufacturing process outlined in the main text and in [4]. Specifically, facets are laser-cut in a 350 μm thick sheet of Mylar and adhered to a thinner sheet using a double-sided tape with a 2.5 mm spacing, constituting the flexural hinge. While keeping one of the facets vertically fixed, we apply a variable point load to the geometrical center of the free facet and extract the opening angle of the fold Ψ (see Fig.1a). The opening angle in the absence of load is set to $\Psi_0 \approx 113°$ for all the tests, but note that the stiffness was found independent of Ψ_0 in the previous study of [4]. The fold acts as a torsional spring between two rigid facets, exhibiting a linear relationship between the torque applied T (accounting for the weight of the hanging facet as well) and the angular deviation $\Psi - \Psi_0$ (see Fig.1b). The stiffness is extracted from the slope as $T = \kappa L(\Psi - \Psi_0)$, with $L = 4$ cm the crease length. Table 1 displays κ values for the four thin sheets. As the different mylar sheets were purchased from different companies, we did not investigate stiffness dependence on the thickness. Repeatability and robustness were assessed by measuring κ for eight folds from a 50 μm sheet, resulting in an 8% variability based on standard deviation relative to the mean value.

The finite number of sheet thicknesses available for fold manufacturing imposes limitations on achievable stiffness values, particularly in the context of the inverse design process requiring arbitrary κ. To address this constraint, we employ a strategy inspired by prior work [7] and introduce slits in the folds. Slits with length $l_s = 5$ mm are evenly distributed along the crease length L_0, and span its width (see Fig.2a). Adjusting their

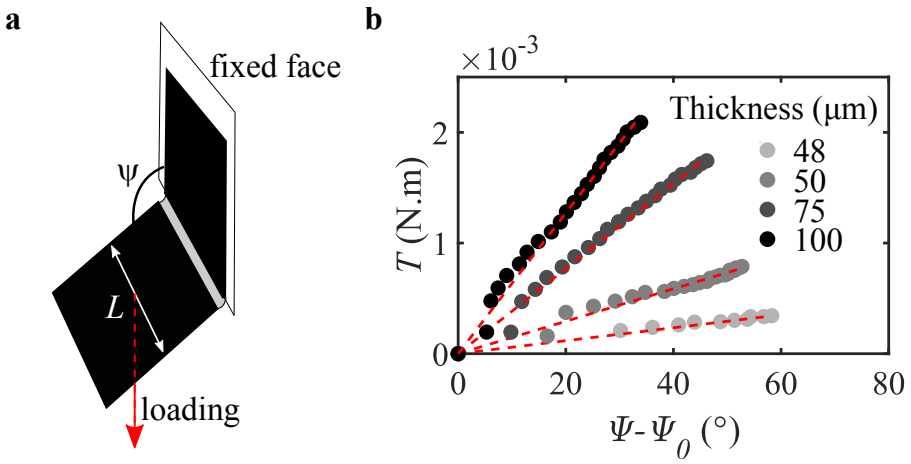

Figure 1: (a) Fold stiffness is assessed by measuring the opening angle Ψ of a single fold while applying a variable point force at the center of the free facet. (b) Torque T as a function of the angular deflection relative to the rest angle $\Psi - \Psi_0$, for folds made from sheets of varying thickness.

Sheet Thickness (μm)	48	50	75	100
Fold stiffness κ(N) $\times 10^{-3}$	8	19	53	92

Table 1: Stiffness measured for folds made from sheets with different thickness.

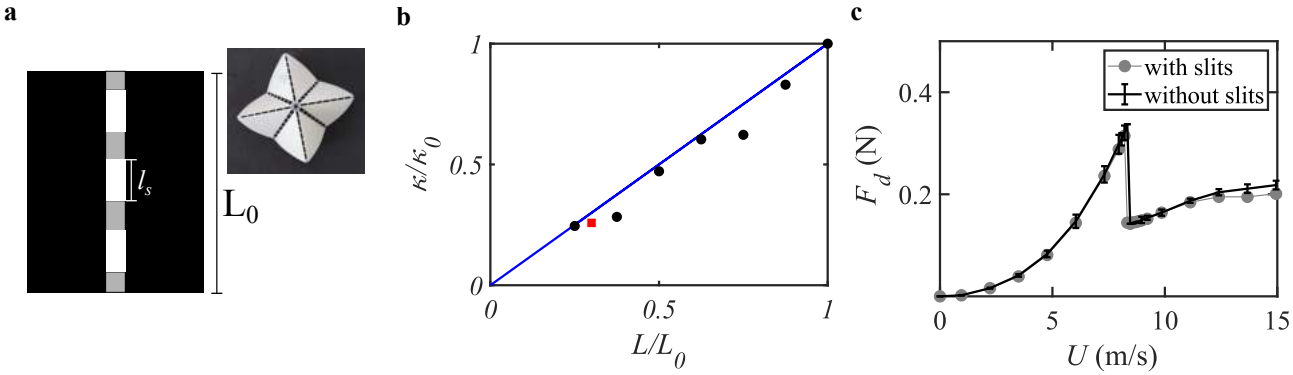

Figure 2: (a) To adjust fold stiffness, slits of varying length l_s and number n_s, spaced at 5 mm intervals, are incorporated into the crease. (b) Stiffness κ of a slitted fold, relative to the uncut fold stiffness κ_0, as a function of the ratio of the remaining material length $L = l_s n_s$ to the total length L_0, for a fold made from a 75 μm sheet. The red point corresponds to a stiffness that mimics an uncut fold made from a 50 μm sheet. (c) Evolution of the drag force as a function of the flow velocity for two origami units with the same fold stiffness: one with slitted folds (grey curve, corresponding to the red point in (b)) and one with unslitted folds (black curve, same curve as in Fig.3a). For both specimens, $R = 5$ cm and $\theta_0 = 41^o$.

number n_s modulates the effective length of the fold $L = L_0 - n_s l_s$, thereby changing its stiffness and facilitating the attainment of diverse κ values. As shown in Fig.2b, the stiffness of a slitted fold scales linearly with its effective length, with a 7% deviation from the expected linear relationship.

To verify the minimal impact of slits on the interaction of the origami unit with the flow, we conducted experiments with two specimens —one with slitted folds and another with unslitted folds— both having the same stiffness. The stiffness of folds made from a 50 μm thick sheet is replicated using a 75 μm thick sheet with slits corresponding to the red point in Fig.2b. As shown in Fig.2c, these two specimens exhibit nearly identical drag curves, with only a slight deviation at higher flow velocities. This similarity indicates that the slits have minimal impact on the unit's performance in the flow.

1.2 Uncertainties and repeatability of the experiments

Drag measurement were acquired using a force sensor (SIXAXES, FX2.6, No 1026, range ± 5 N) with a sensitivity of ±0.001 N. Significant variations in the drag force are observed due to flow unsteadiness, which are mitigated by averaging the data over a 30-second period with a data acquisition rate of 1024 Hz. To estimate

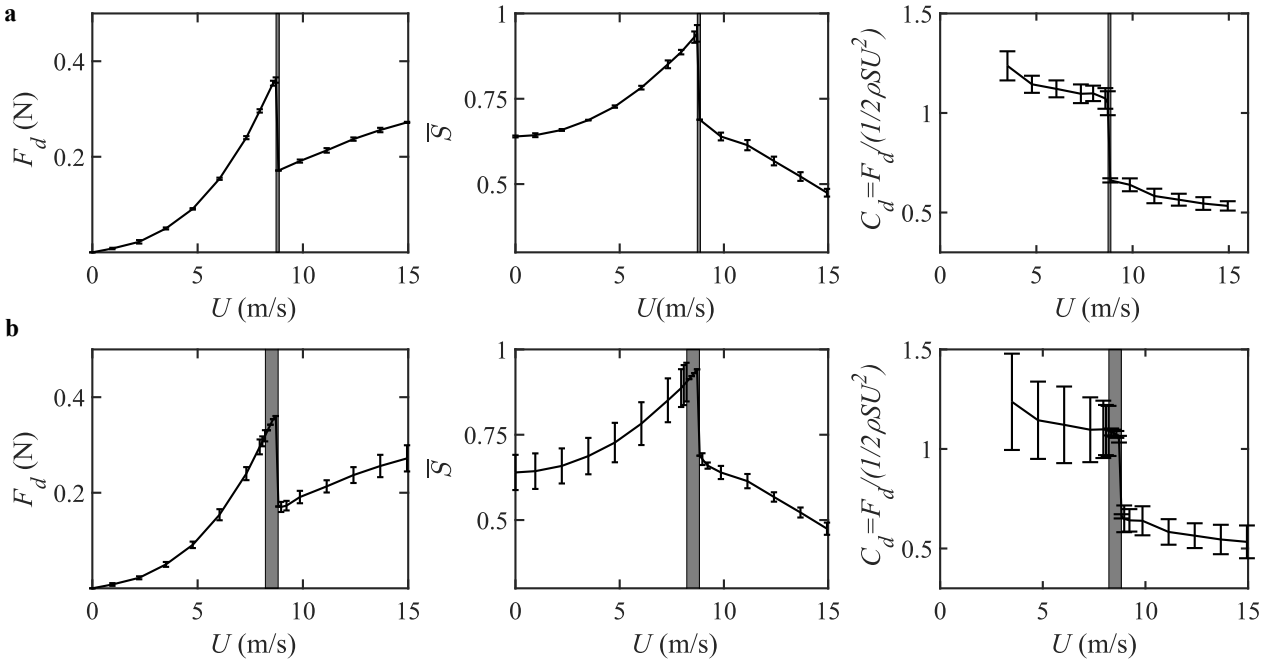

Figure 3: Evolution of drag force F_d, dimensionless projected area $\overline{S} = S/\pi R^2$, and drag coefficient $C_d = F_d/(1/2\rho SU^2)$ with flow speed U, for origami specimens with $R = 5$ cm, $\kappa = 19 \times 10^{-3}$ N and $\theta_0 = 41°$. In (a), the same cell is tested three times, with re-annealing between each iteration. In (b), experiments are replicated across five independent cells sharing the same parameters. Error bars indicate the standard deviation (the grey zone denotes the variation in critical speed). The error bars for C_d are inferred from the variations in S, F_d and U.

the uncertainty in these averaged force measurements, we conducted three repetitions of the experiments on the same unit. Before each test, the unit underwent an hour of re-annealing in the oven, followed by an additional hour of cooling at room temperature to ensure a consistent initial cell configuration. The standard deviations for the measurements are depicted in Fig.3a, and indicates a relative variation in drag force within 2%.

The projected area is measured using a Sony SLT-A65V camera, that capture images of size 6000×4000 pixels with one pixel corresponding to 0.2 mm. The resolution of the images introduces a relatively small source of uncertainty, as does the image analysis process for extracting the frontal area. Repeatability tests with the same cell, tested three times, result in a relative variation within 2% for the dimensionless projected area, as shown in Fig.3a. Another source of uncertainty arises from capturing a single image to measure the instantaneous projected area, while vibrations were observed in some cases. To assess these vibrations, we conducted experiments recording the unit's behavior with a camera over 5 seconds at a frame rate of 100 fps. The standard deviation of the frontal area for each velocity increment is represented by the error bars in Fig.4. Measurements over a longer 20-second period (using a lower frame rate of 30 fps due to analysis duration

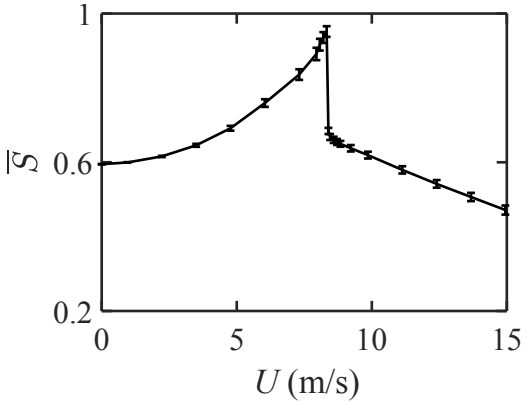

Figure 4: Projected area as a function of the flow velocity for a waterbomb unit with $R = 5$ cm, $\kappa = 19 \times 10^{-3}$ N and $\theta_0 = 41^o$. The area values are averaged over 5 seconds, recorded with camera with a frame rate of 100 fps, and the error bar represent the standard deviation.

constraints) also exhibited similar variations. We observe increased area fluctuations as the cell approaches the unstable flat state in Fig.4, which is associated with more significant vibrations. However, the relative deviation remains below 3%. These vibrations likely contribute to the variation in the critical velocity for snapping, leading to earlier snap-through. Nevertheless, the repeatability tests of Fig.3a show a small relative variability in critical speed within 2%.

To further test the reproducibility of the fabrication process and the effect of origami variability on drag, we repeated experiments in the wind tunnel for five distinct units fabricated with identical parameters $R = 5$ cm, $\kappa = 19\times10^{-3}$ N and $\theta_0 = 41°$ (which is the common configuration for all three parametric series of origami cells). Fig.3b presents the error bars for drag and the cell projected area, corresponding to the standard deviation. The grey region denotes the variation in the critical speed for snap-through U_c. The associated relative errors are of the order of 10%, 9.5% and 5%, respectively for F_d, $S/\pi R^2$ and U_c. The predominant source of variability thus comes from the fabrication process rather than the experimental measurement method, notably concerning the detection of the snap-through threshold.

2 Kinematics and mechanical properties of the waterbomb base

2.1 Folding kinematics

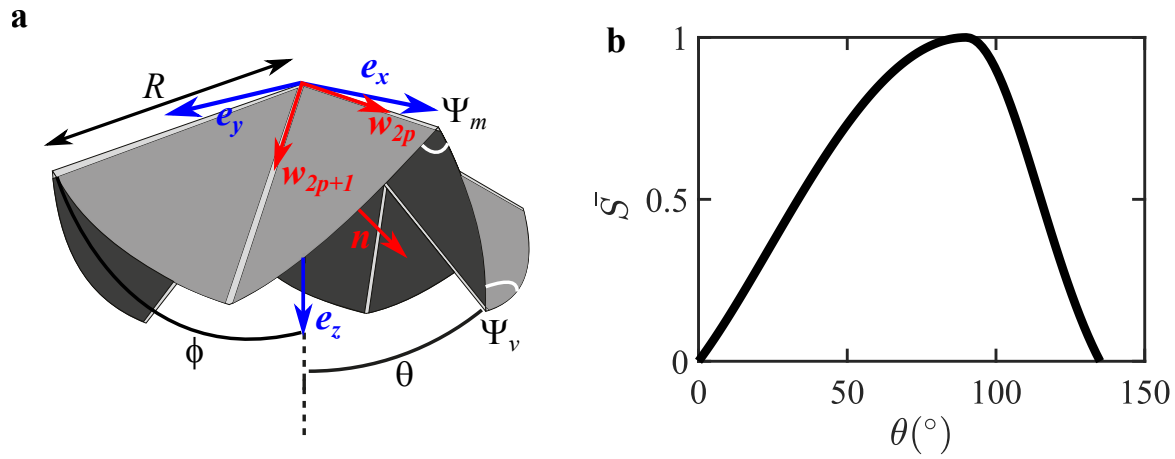

Figure 5: (a) Waterbomb base, featuring the various relevant angles (see text), and the unit vectors $\boldsymbol{w_{2p}}$ and $\boldsymbol{w_{2p+1}}$ aligned along the mountain and valley creases. (b) Variation of the dimensionless projected area $\overline{S} = S/\pi R^2$ with the opening angle θ.

The folding kinematics of the waterbomb base have been described extensively in previous work [3, 1, 4], and we only recapitulate here the main elements. The traditional version comprises a disk with a radius R, featuring $N = 8$ folds that radiate from the center and are separated by equal sector angles $\alpha = 2\pi/N$. We assume that the facets are rigid with deformation localized at the creases and that the deformation is symmetric, meaning that all the mountain folds deflect by the same amount, and the same holds for the valley folds. Folding then reduces to one degree of freedom mechanism, which can be described by a single parameter, selected here as the angle θ made by a valley fold with the central axis passing through the vertex of the unit (see Fig.5a).

In line with [1, 4], the folding kinematics is derived by using the unit vectors $\boldsymbol{w_{2p}}$ and $\boldsymbol{w_{2p+1}}$, which are aligned respectively with the mountain and valley creases, with $p = 0, ..., N/2$ and $\boldsymbol{w_0} = \boldsymbol{w_N}$. The components of these vectors in the Cartesian system coordinate, shown in Fig.5a, are:

$$\begin{aligned} \boldsymbol{w_{2p}} &= (\sin\phi\cos 2p\alpha, \sin\phi\sin 2p\alpha, \cos\phi) \\ \boldsymbol{w_{2p+1}} &= (\sin\theta\cos(2p+1)\alpha, \sin\theta\sin(2p+1)\alpha, \cos\theta) \end{aligned} \tag{1}$$

with ϕ the angle between valley folds and the central z-axis (see Fig.5a). The rigid facet assumption, expressed as $\boldsymbol{w_{2p}}.\boldsymbol{w_{2p+1}} = \cos\alpha$, establishes a relationship between θ and ϕ :

$$\cos\phi\cos\theta - \cos\alpha(1 - \sin(\phi)\sin(\theta)) = 0 \tag{2}$$

Equation 2 can be rewritten as :

$$\phi(\theta) = \begin{cases} \arccos\left(\dfrac{\cos\alpha\cos\theta}{1+\sin\alpha\sin\theta}\right) & \text{for } 0 \le \theta \le \pi/2 \\ \arccos\left(\dfrac{\cos\alpha\cos\theta}{1-\sin\alpha\sin\theta}\right) & \text{for } \pi/2 < \theta \le \pi - \alpha \end{cases} \tag{3}$$

The first relation describes the opening kinematics and the second one describes the closing past the flat configuration $\theta = \pi/2$. The angles of the mountain and valley folds denoted as ψ_m and ψ_v respectively, can be expressed in terms of θ and ϕ [1]:

$$\begin{aligned} \cos\psi_v &= \cos 2\theta \\ \cos\psi_m &= \cos 2\phi \end{aligned} \tag{4}$$

Their expression as a function of θ thus differs as well on each side of the flat configuration.

Note that in the main text, we use S, the projected area in the xy-plane, to characterize the shape reconfiguration of the unit. Its non-dimensional expression (normalizing by the area of the flat state πR^2) is given by:

$$\overline{S} = \frac{S}{\pi R^2} = \boldsymbol{n}.\boldsymbol{e_z} = \sin\theta \sin\phi \tag{5}$$

Where $\boldsymbol{n}$ is the unit vector normal to the facet defined by vectors $\boldsymbol{w_{2p}}$ and $\boldsymbol{w_{2p+1}}$:

$$\boldsymbol{n} = \frac{\boldsymbol{w_{2p}} \times \boldsymbol{w_{2p+1}}}{||\boldsymbol{w_{2p}} \times \boldsymbol{w_{2p+1}}||} \tag{6}$$

The evolution of the dimensionless projected area $\overline{S}$ with the opening angle θ as the unit opens up and closes is shown in Fig.5b.

2.2 Elastic potential energy and stable states

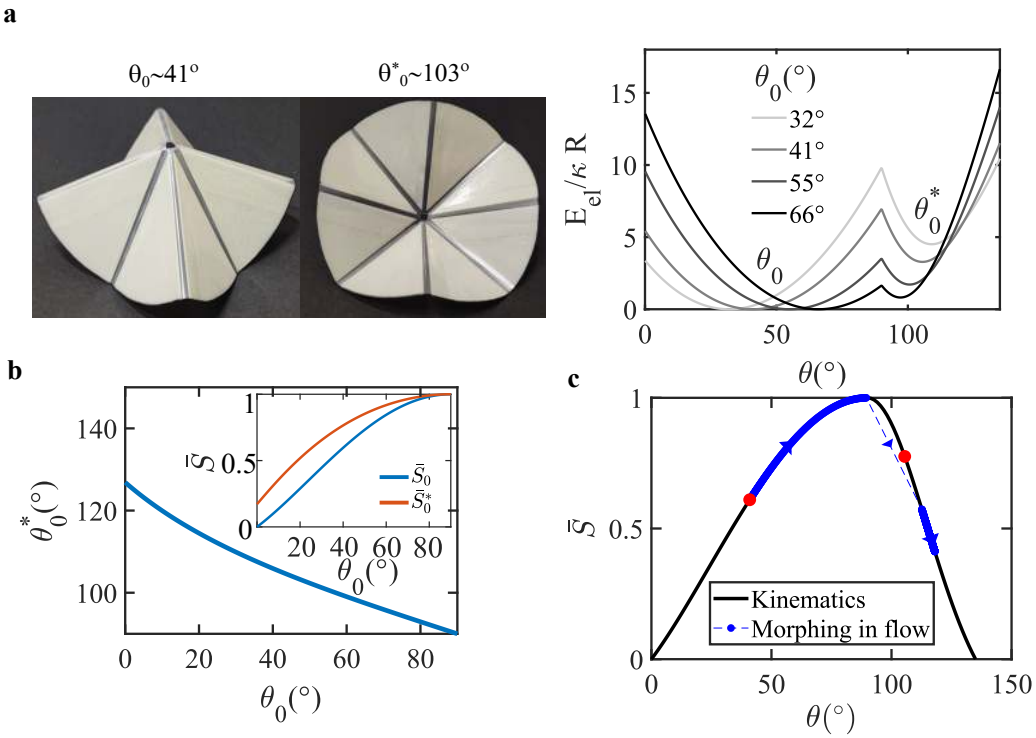

Figure 6: (a) Elastic potential energy landscape for the waterbomb base, displaying two stable states with angles θ_0 and θ_0^*, separated by an unstable planar state, for varying θ_0. On the right, images of the two stable states for a unit with $\theta_\circ = 41°$. (b) Evolution of θ_0^* with θ_0. Corresponding dimensionless projected areas $\overline{S_0}$ and $\overline{S_0^*}$ are shown in the inset. (c) Theoretical prediction for the shape reconfiguration (expressed in terms of θ and $\overline{S}$) of an origami unit exposed to a flow with increasing velocity (blue curve). It is computed for a waterbomb cell with $\theta_0 = 41^o$ and varying Cauchy number $C_y = 0 - 50$. The black curve represents the waterbomb folding kinematics and the red dots denote the two stable states θ_0 and θ_0^*.

The mechanical behavior of the origami unit is modeled by treating its folds as elastic hinges with rigidity κ and length R. The elastic potential energy comprises contributions from the $N/2$ mountain folds and the $N/2$ valley folds:

$$E_{el} = \frac{\kappa R}{2}\frac{N}{2}[(\psi_m - \psi_m^0)^2 + (\psi_v - \psi_v^0)^2] \tag{7}$$

Here, ψ_m^0 and ψ_v^0 denote the rest angles of the mountain and valley folds. Using the angle expressions from Eq.3 and Eq.4, E_{el} can be expressed as a function solely of θ and θ_0. Fig.6a shows the evolution of the normalized

elastic potential energy $E_{el}/\kappa R$ as a function of θ for various rest angles θ_0. The energy landscape features two wells corresponding to two stable states, which are separated by an unstable flat state at $\theta = \pi/2$. Pictures of an origami unit in its two stable configurations, characterized by angle θ_0 and θ_0^*, are shown in Fig.6a. Smaller values of θ_0 (corresponding to compact states, light grey curve) have a higher energy barrier to overcome to transition to the second stable state. The second equilibrium configuration is also correspondingly more compact (higher θ_0^*), resulting in a more pronounced shape change upon snapping. The relationship between θ_0^* and θ_0 can be numerically determined through energy minimization for a given θ_0, and it is illustrated in Fig.6b. The inset of Fig.6b also shows the evolution of the dimensionless projected area $\overline{S_0}$ and $\overline{S_0^*}$ for the two stable states, showing that the two states are not the mirror image of each other and that the second one is always slightly more open than the first one.

The blue curve in Fig.6c depicts the morphing of a waterbomb base along its folding pathway (black curve) when subjected to a flow with increasing speed U. This evolution is computed using the fluid-elastic model detailed in the next section. In the absence of flow, the unit resides in its first stable state (denoted by the red point). As U rises, it unfolds, and upon reaching the flat unstable state ($\overline{S} = 1$), it abruptly snaps towards a state that is more compact than the state $\overline{S_0^*}$ due to the fluid loading.

3 Fluid-structure model

3.1 Theoretical model

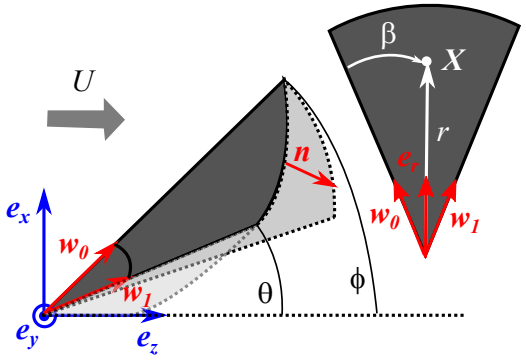

Figure 7: Parameterization used to compute the work of fluid forces on a facet defined by the unit vectors $\boldsymbol{w_0}$ and $\boldsymbol{w_1}$.

To model the origami unit's response to a flow, we adopt the same energy-based approach from prior work on the waterbomb unit's closing dynamics of the waterbomb in a flow [4]. We recapitulate here the main elements and extend it to include snapping. The unit's static equilibrium in a flow is determined by minimizing its energy $E_{el} - W$, which includes both the elastic potential energy E_{el}, and the work done by fluid forces W as the unit deforms from its initial rest state θ_0 to an angle θ:

$$E_{el} - W = \frac{\kappa R}{2}\frac{N}{2}[(\psi_m - \psi_m^0)^2 + (\psi_v - \psi_v^0)^2] - N\int_{\theta_0}^{\theta}\int_{S_f} \rho(\boldsymbol{U}.\boldsymbol{n})^2 dS_f \boldsymbol{n}.d\boldsymbol{X} \tag{8}$$

Where ρ denotes the density of the fluid and other quantities are introduced later. The second term sums the work done by fluid loading on each facet (with area $S_f = \pi R^2/N$), which is the same for all of the facets due to the symmetry of motion. Fluid pressure forces acting on each surface element of a facet are integrated along the local displacement $d\boldsymbol{X}$. Note that $\boldsymbol{n}$ and $\boldsymbol{X}$ are functions of the folding angle θ, as indicated by the θ-subscripts in Eq.2 and 3 of the paper. For simplicity, we will omit that subscript here. Pressure is modeled using the momentum conservation arguments, following the approach in [2, 5, 6, 4]. It scales with the momentum carried by the flow in the direction perpendicular to the facet $\rho(\boldsymbol{U}.\boldsymbol{n})^2$, with $\boldsymbol{n}$ the normal unit vector as defined in Eq.6.

The trajectory $\boldsymbol{X}$ of each surface element of a facet is obtained from the kinematics analysis presented earlier. We consider the facet of Fig.7 associated with the crease vector field $\boldsymbol{w_0}$ and $\boldsymbol{w_1}$. A point on the facet is localized through the distance $r \in [0, R]$ and polar angle $\beta \in [0, \alpha]$, as shown in Fig.7. Its position vector is expressed as $\boldsymbol{X} = r\boldsymbol{e_r}$ with $\boldsymbol{e_r}$ the radial unit vector. This vector lies in the $(\boldsymbol{w_0}, \boldsymbol{w_1})$ plane and can thus be expressed as a linear combination of these two vectors:

$$\boldsymbol{e_r} = \frac{\boldsymbol{w_0} + C\boldsymbol{w_1}}{||\boldsymbol{w_0} + C\boldsymbol{w_1}||} = \frac{\boldsymbol{w_0} + C\boldsymbol{w_1}}{\sqrt{1 + 2C\cos\alpha + C^2}} \text{ with } C \text{ verifying } \boldsymbol{e_r}.\boldsymbol{w_0} = \cos\beta \tag{9}$$

Note that an error was identified in the calculations presented in [4] (with a missing square root in the denominator in Eq.9, and a mistaken interchange of A and B in Eq.13). Importantly, despite these errors, the overall trends and conclusions of the model remain unchanged. In fact, the corrected equations result in theoretical predictions that align more closely with experimental results in [4].

From Eq.9, the parameter C can be expressed as a function of α and β:

$$C = \frac{-\cos\alpha(\cos^2\beta - 1) + \cos\beta\sqrt{(\cos^2\beta - 1)(\cos^2\alpha - 1)}}{\cos^2\beta - \cos^2\alpha} \tag{10}$$

Deformation of the origami unit by $d\theta$ results in elementary displacements $d\boldsymbol{X}$ for points of the facet :

$$d\boldsymbol{X} = r\frac{d\boldsymbol{e_r}}{d\theta}d\theta = \frac{r d\theta}{\sqrt{1 + 2C\cos\alpha + C^2}}\left(\frac{d\phi}{d\theta}\cos\phi + C\cos\theta\cos\alpha, C\cos\theta\sin\alpha, -\frac{d\phi}{d\theta}\sin\phi - C\sin\theta\right) \tag{11}$$

The work done by fluid forces on all of the facets then writes:

$$W = -\frac{NR^3\rho U^2}{3}\int_{\theta_0}^{\theta}\sin^2\theta\sin^2\phi\left[A\frac{d\phi}{d\theta}\sin\theta + B\sin\phi\right]d\theta \tag{12}$$

With A and B given by:

$$A = \int_0^{\alpha}\frac{1}{\sqrt{1 + 2C\cos\alpha + C^2}}d\beta \quad \text{and} \quad B = \int_0^{\alpha}\frac{C}{\sqrt{1 + 2C\cos\alpha + C^2}}d\beta \tag{13}$$

The equilibrium angle θ of the unit in the flow is then given by the zeros of $d(E_{el} - W)/d\theta$, which yields the equation:

$$(\psi_m - \psi_m^0)\frac{d\psi_m}{d\theta} + (\psi_v - \psi_v^0)\frac{d\psi_v}{d\theta} + \frac{2}{3}C_y\sin^2\theta\sin^2\phi\left[A\frac{d\phi}{d\theta}\sin\theta + B\sin\phi\right] = 0 \tag{14}$$

Where $C_y = \rho U^2R^2/\kappa$ is the same Cauchy number as defined for experiments. Eq.14 is numerically solved using the nonlinear system solver *fsolve* of Matlab. The Cauchy number is varied linearly from 0 to 50 in 500 steps, and the solver utilizes the value of θ obtained at the previous iteration as a starting point (initializing at θ_0 for $C_y = 0$). As θ approaches the flat state beyond $\pi/2 - \epsilon$, with $\epsilon = 0.01$ radians, Eq.14 is then solved using the new set of equations describing the angles in the closing part of the kinematics (given in Eq.3) with first starting point at $\pi/2 + \epsilon$.

From the equilibrium angle θ, we obtain the dimensionless projected surface $\overline{S}$ using Eq.5, and the dimensionless drag force by projecting pressure fluid forces in the direction of the flow $\boldsymbol{e_z}$:

$$\overline{F_d} = F_d/\kappa = \pi C_y\sin^3\theta\sin^3\phi \tag{15}$$

3.2 Effect of mechanical model simplifications on drag predictions

In this section, we compare the cell's mechanical response to the idealized model, which assumes mechanical properties are dictated by folds modeled as torsional springs. We then evaluate how deviations from this model affect drag behavior to understand the contribution of these simplifications to the discrepancies observed between experiments and theoretical predictions of Fig.3a of the main text.

We conducted force-deflection tests on a waterbomb unit, following the protocols outlined in [3] and briefly described here. We record the force as the vertex is deflected downward towards the unstable equilibrium position using a tensile testing machine. Two tests were performed on each side of the flat state. The vertex is connected to the force sensor by a rod with the same attachment used in the flow experiments to replicate the mechanical conditions. The unit is either resting on a low-friction flat acrylic plate or on an acrylic support to maintain consistent contact points on the valley folds for both tests. The results are shown in Fig.8a, with colors differentiating the two tests on either side of the equilibrium position. The experimental data are compared to the theoretical force-deflection relationship derived through virtual work analysis for an ideal cell (dashed line, see [3]). The experimental results are similar to those reported in [3], though there is better alignment with the theoretical model. Deviations are observed near the unstable flat state, showing a softening of the unit that may be due to the contribution of the vertex, which is likely more pronounced near the flat state than in the vicinity of the equilibrium states, or could be attributed to fabrication imperfections. As noted by [3], the experimental data align most closely with the ideal waterbomb base when it is near the first stable position, which is the state in which it was manufactured. Imperfections may become more pronounced as the unit deviates further from this position. Nonetheless, the overall agreement is reasonable.

To estimate the effect of these deviations on flow behavior, we modified the fluid-structure model by replacing the elastic potential energy of the ideal unit E_{el} in Eq.8 with the one obtained experimentally by integrating the force-deflection data from the tensile test of Fig.8a. The prediction of the modified model for drag evolution is

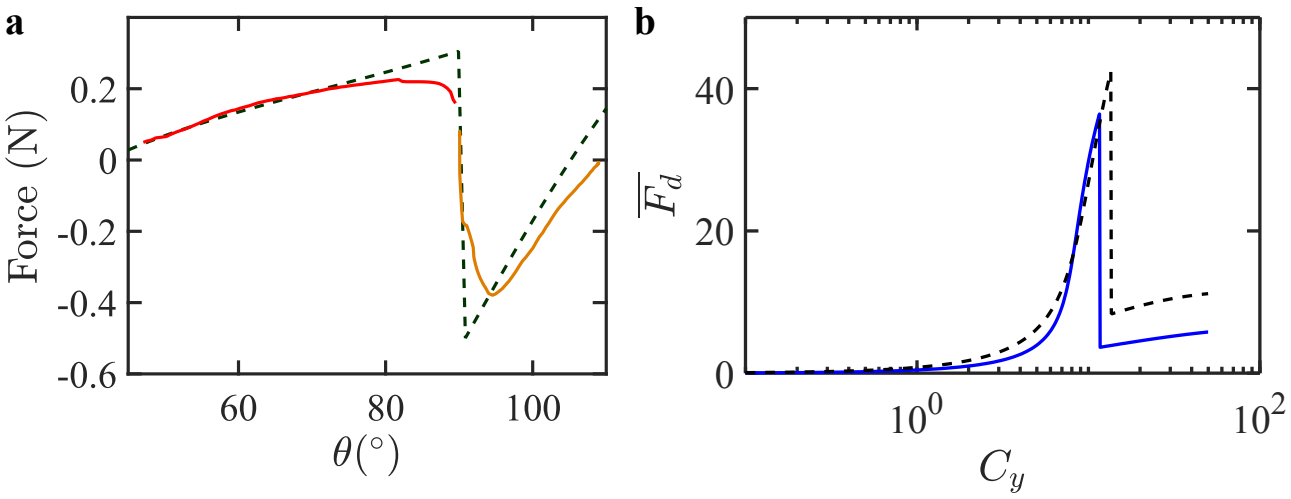

Figure 8: (**a**) Force-deflection measurements on a waterbomb unit ($R = 5$ cm, $\kappa = 19 \times 10^{-3}$ N and $\theta_0 = 41^o$), with the two colors differentiating tests starting from each stable state. It is compared to the theoretical prediction of an ideal waterbomb base (dashed line). (**b**) Theoretical prediction for the dimensionless drag $\overline{F_d}$ as a function of the Cauchy number C_y, obtained using the potential elastic energy of the cell derived from tensile test experiments (solid blue line), and compared to that of Fig.3a of the main text (dotted black line).

shown in Fig.8b and compared to the ideal-unit model. The softening near the flat state leads to snap-through at a lower critical speed and a lower peak drag. Although deviations in origami mechanics from the ideal description may partly explain the discrepancies between the model and experimental results in Fig.3a of the main text, they do not appear to be the main factor.

4 Effect of the number of folds

While the present manuscript focuses on the traditional version of the origami waterbomb with $N = 8$ folds, this parameter represents an interesting addition to expand the parameter space. In this section we discuss the effect of N on the kinematic and mechanical properties of the waterbomb base, and how it affect the drag behavior.

4.1 Elastic potential energy and stable states

Fig.9a shows the elastic potential energy landscape derived from the kinematic and mechanical description in Section 2, for different values of N. Increasing the number of folds raises the potential energy barrier that the unit must overcome to transition to the second stable state. While all configurations share the same rest angle θ_0 in the first stable state (defined as the angle between the valley folds and the central axis), the second equilibrium configuration becomes more compact with a higher number of folds (higher θ_0^*). Note that, unlike other parameters (R, κ and θ_0), changing the number of folds alters the folding kinematics, as highlighted by the different evolution of the dimensionless projected area $\overline{S}$ with the opening angle in Fig.9b.

4.2 Influence of number of folds on drag

To experimentally characterize the effect of the number of folds on drag, we conducted flow experiments for different $N = 6-12$, while keeping the size, stiffness, and rest angle constant at $R = 5$ cm, $\kappa = 19 \times 10^{-3}$ N and $\theta_0 = 41°$, respectively. The results, presented in Fig.9a-b, show a trend similar to that observed with changes in θ_0. Specifically, a greater number of folds delays snapping to higher velocities, leading to a higher peak drag. It also produces a larger collapse in frontal area post-snapping, thus causing a higher drag jump, analogous to what is seen with smaller θ_0. These observations are consistent with Fig.9, which indicates that N alters the energy barrier for snap-through and the degree of opening of the second stable state, much like θ_0. However, a key distinction is that units with different values of N display comparable evolution of drag and frontal area after snapping, whereas units with varying θ_0 exhibit noticeable differences. Drag results are plotted in non-dimensional form as a function of the Cauchy number in Fig.9c, and compared with our theoretical predictions shown in Fig.9d. The model captures the influence of the number of folds on drag characteristics, in terms of the peak drag, the critical velocity for snapping, and the similar drag evolution post-snapping.

We chose not to include the number of folds in our inverse design framework because it can only take a finite number of values, as it must be an even integer, and large values of N are challenging to implement

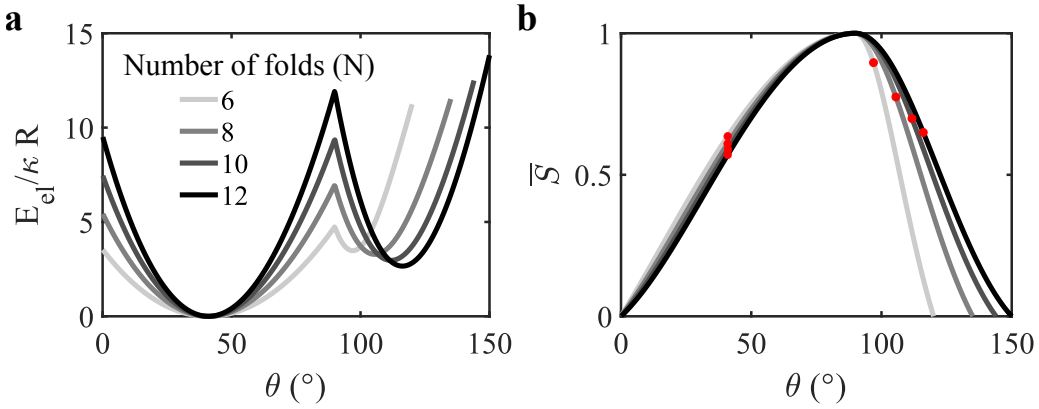

Figure 9: (**a**) Elastic potential energy landscape for the waterbomb base with a varying number of folds N and $\theta_0 = 41^o$. (**b**) Evolution of the dimensionless projected area, illustrating different folding kinematics. The red dots indicate the two stable states on either side of the unstable flat state.

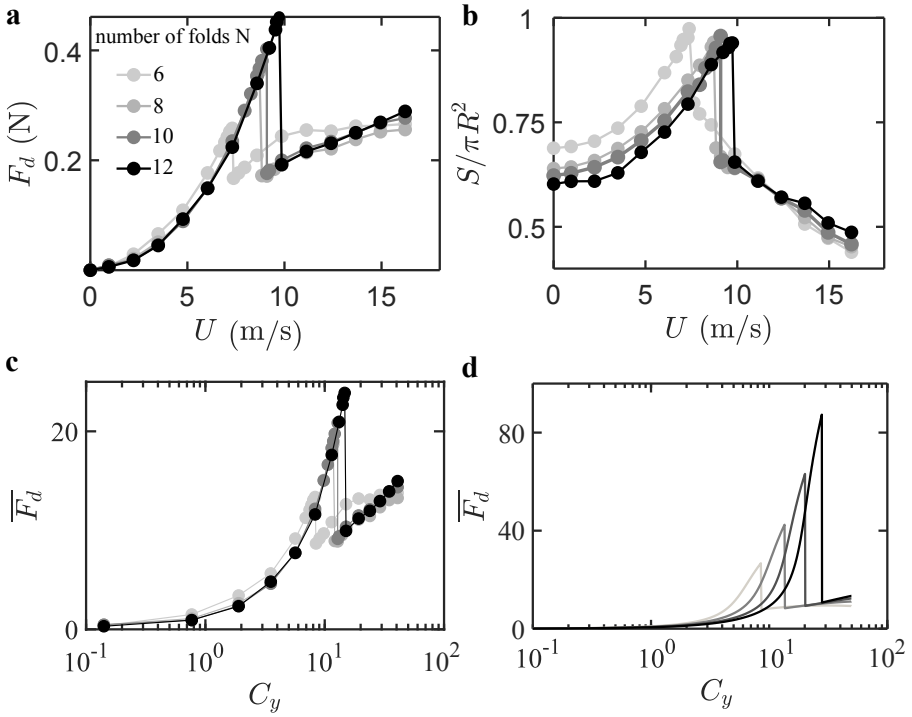

Figure 10: **Influence of the number of folds on drag**. Evolution of (**a**) the drag force F_d and (**b**) the dimensionless frontal area $S/\pi R^2$ as a function of flow velocity U for origami units with different number of folds N. (**c**) Experimental drag results are recast in dimensionless form as a function of the Cauchy number, and (**d**) compared to theoretical prediction.

experimentally. This made it less suitable for our current reverse engineering study. Nonetheless, given its distinctive effect post-snapping, it could serve as a valuable complementary parameter for controlling the rate at which drag increases with velocity post-jump, for example.

5 Inverse design

The objective of the inverse problem is to identify the optimal parameter set (R, κ, θ_0) that achieves a collapse in drag, targeting a peak drag force $F^t_{d,max}$ and a specific jump value ΔF^t_d at a critical flow speed U^t_c. The optimization uses the fluid-elastic model described earlier, which predicts drag evolution with flow speed based on given cell parameters. Using the *trust region dogleg* algorithm of fsolve solver from Matlab, the system of equations $F_d - F^t_{d,max} = 0$, $\Delta F_d - \Delta F^t_d = 0$ and $U_c - U^t_c = 0$ is solved for the variables (R, κ, θ_0). The algorithm converges to a single solution meeting the constraints, with a maximum residual of $O(10^{-19})$ within a hundred iterations. Note that the optimization algorithm cannot produce θ_0 below 25^o, likely due to the simplified representation for fluid forces considered in the model, leading to an inflection point in the $F_d(C_y)$ curve for small θ_0.

Target values			**Corresponding cell parameters**		
$F^t_{d,max}$ (N)	U^t_c (m/s)	ΔF^t_d (N)	κ ($\times 10^{-3}$N)	R (cm)	$\theta_0(^\circ)$
0.8	4	0.6	21	4.6	47
0.8	7	0.6	21	6.5	47
0.8	10	0.6	21	11.4	47
0.8	7	0.5	27	6.5	56
0.8	7	0.7	16	6.5	33
0.65	7	0.6	11	5.9	25
0.95	7	0.6	32	7.1	56

Table 2: Fabrication parameters produced by the optimization algorithm, for given target drag parameters.

The target values $(F^t_{d,max}, \Delta F^t_d, U^t_c)$ used, along with the corresponding cell parameters, are presented in Table 2. When varying U_c (while keeping the other two drag features constant), cells with the same radius but different κ and θ_0 are obtained. Interestingly, selectively varying ΔF_d is achieved by adjusting θ_0 and κ while maintaining a constant R.

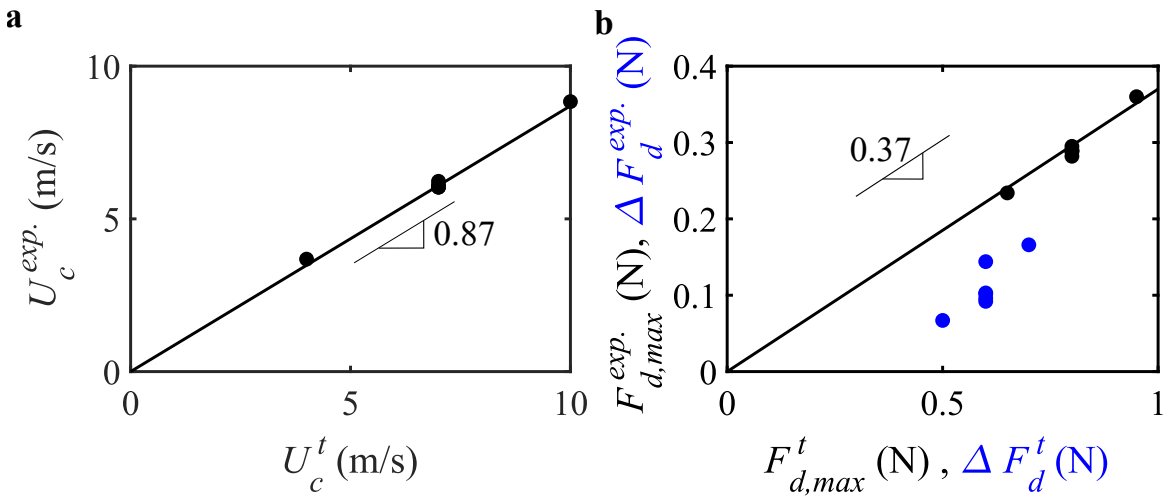

Figure 11: Relationship between the target values and the values obtained experimentally for (a) the critical speed U_c, and (b) the drag peak $F_{d,max}$ (in black) and jump ΔF_d (in blue).

The physical samples, fabricated using the optimized cell parameters from Table 2, successfully exhibit the desired selective variation of each drag characteristic (see Fig.4 of the main text). Experimentally obtained

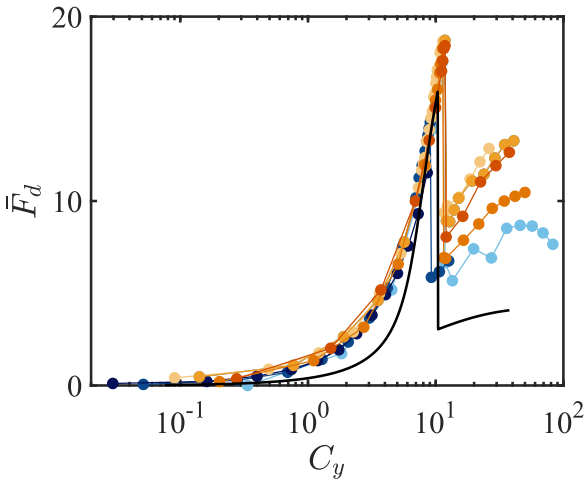

Figure 12: Fig.3 of the main text is reproduced with the theoretical curve modified by re-scaling for flow velocity and drag using the proportionality factors from Fig.11.

values of $(F_{d,max}, \Delta F_d, U_c)$ are compared to the target values in Fig.11. While the experimental values of U_c are reasonably close to the target ones (see Fig.11a), values of $F_{d,max}$ and ΔF_d are notably lower than the target values in Fig.11b. However, this disparity is expected given the semi-quantitative agreement between the model and experiments in Fig.3 of the main text, where the model tends to overestimate drag. From the linear relationships depicted in Fig.11, we can extract proportionality factors between target values and the ones experimentally obtained, for both flow speed and drag (using $F_{d,max}$ values). In Fig.12, the model prediction from Fig.3 of the main text is re-plotted by re-scaling drag and flow speed using these proportionality factors, showing a good alignment with the experimental data. Deviations observed in the inverse design implementation are thus consistent with the initial level of agreement between experiment and theory. Using a more refined fluid-elastic model is therefore expected to improve the closeness to the target in the inverse design process. Note that the theoretical ΔF_d does not align satisfactorily with experimental data in Fig.12, as the deviation between experimental and target drag value cannot be captured by a single proportionality factor for both $F_{d,max}$ and ΔF_d in Fig.11b.

6 Multiple units

References

[1] V. Brunck, F. Lechenault, A. Reid, and M. Adda-Bedia. Elastic theory of origami-based metamaterials. *Phys. Rev. E*, 93(3):033005, 2016.

[2] F. Gosselin, E. de Langre, and B. A. Machado-Almeida. Drag reduction of flexible plates by reconfiguration. *J. Fluid Mech.*, 650:319, 2010.

[3] B. H. Hanna, J. M. Lund, R. J. Lang, S. P. Magleby, and L. L. Howell. Waterbomb base: a symmetric single-vertex bistable origami mechanism. *Smart Mater. Struct.*, 23(9):094009, 2014.

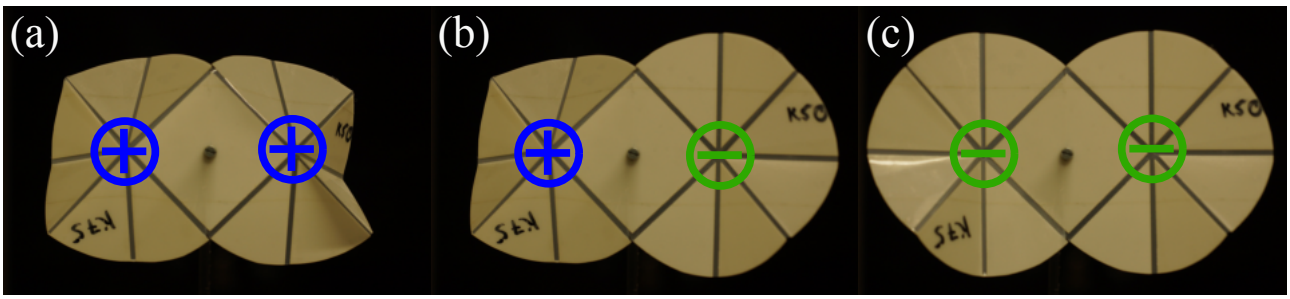

Figure 13: Different states of the multistable assembly of the waterbomb units, Frontal view. (a)Both the units are in the first stable state(++). (b)Unit of lower stiffness in a second stable state(-) and higher stiffness in the first stable state(+). (c) Both the units are in their second stable state(–).

[4] T. Marzin, E. de Langre, and S. Ramananarivo. Shape reconfiguration through origami folding sets an upper limit on drag. *Proc. R. Soc. A*, 478(2267):20220592, 2022.

[5] L. Schouveiler and A. Boudaoud. The rolling up of sheets in a steady flow. *J. Fluid Mech.*, 563:71, 2006.

[6] L. Schouveiler and C. Eloy. Flow-induced draping. *Phys. Rev. Lett.*, 111(6):064301, 2013.

[7] F. Zuliani, C. Liu, J. Paik, and S. M. Felton. Minimally actuated transformation of origami machines. *IEEE Robot. Autom. Lett.*, 3(3):1426–1433, 2018.